AIAA JOURNAL
Vol. 36, No. 11, November 1998

Tetrahedral Unstructured Navier–Stokes Method for Turbulent Flows

Neal T. Frink*
NASA Langley Research Center, Hampton, Virginia 23681-0001

A method is presented for solving the Navier–Stokes equations for turbulent flow problems on three-dimensional unstructured grids. Spatial discretization is accomplished by a cell-centered, finite volume formulation using an accurate linear reconstruction scheme and upwind flux differencing. Time is advanced by an implicit backward Euler time-stepping scheme. Flow turbulence effects are modeled by the Spalart–Allmaras one-equation model (Spalart, P. R., and Allmaras, S. R., "A One-Equation Turbulence Model for Aerodynamic Flows," AIAA Paper 92-0439, Jan. 1992), which is coupled with a wall function to reduce the number of cells in the sublayer region of the boundary layer. A systematic assessment of the method is presented to devise guidelines for more strategic application of the technology to complex problems. The assessment includes the accuracy in predictions of the skin-friction coefficient, law-of-the-wall behavior, and surface pressure for a flat-plate turbulent boundary layer and for the ONERA M6 wing under a high-Reynolds-number, transonic, separated flow condition.

Introduction

SIGNIFICANT advancements are being made toward solving complex viscous flows on three-dimensional configurations using unstructured-grid methodology.[1–8] Whereas solving such flows on highly stretched tetrahedral cells is considerably more difficult than on hexahedral cells, the primary advantage is derived from the greatly reduced grid generation times. Reference 9 has demonstrated that viscous grids can be easily generated on complex shapes by the advancing front/advancing layers methodology. It is anticipated that, in the near future, viscous tetrahedral grids will be generated on complex geometries in a matter of days, as are inviscid tetrahedral grids today.

The viscous, tetrahedral-based unstructured flow solution methodology is maturing along two tracks: node-centered and cell-centered schemes, each with its relative merits. Node-centered schemes exploit an efficient edge-based data structure and have demonstrated multigrid and parallel computer implementations[2,5] but generally require large tetrahedral grids. Cell-centered schemes exploit geometric features of tetrahedra for constructing accurate spatial reconstruction schemes and provide comparable accuracy with fewer tetrahedra but have not been extended to multigrid and have exhibited some limitations in solution stability.

There is a need for systematic assessments of the accuracy and behavior of the various schemes. The present work focuses on an assessment of the upwind, tetrahedral cell-centered finite volume scheme of Ref. 10. This method is extended herein to include the Spalart–Allmaras one-equation turbulence model and the coupling of that model with a wall function to reduce the number of cells in the sublayer region of the boundary layer. It is anticipated that the wall function approach may be applicable to three-dimensional separated flows because flow is not stagnant along separation lines.

The assessments will be derived from the flat-plate boundary-layer problem and the ONERA M6 wing at a high-Reynolds-number, transonic, separated flow condition. Key issues will be addressed related to applying a tetrahedral-based, cell-centered Navier–Stokes method to turbulent flow problems. The objectives of the study are to 1) assess the accuracy of computing turbulent flow pressure distributions and skin-friction coefficients with tetrahedral cells; 2) investigate the accuracy and utility of a wall function formulation for computing three-dimensional, high-Reynolds-number, transonic, separated flow with tetrahedral cells; 3) establish guidelines for generating unstructured, tetrahedral viscous grids for solving turbulent flow problems accurately and efficiently; and 4) demonstrate a mesh sequencing strategy for accelerating solution convergence.

Presented as Paper 96-0292 at the AIAA 34th Aerospace Sciences Meeting, Reno, NV, Jan. 15–18, 1996; received March 14, 1996; revision received July 10, 1998; accepted for publication July 27, 1998.

*Senior Research Engineer, Configuration Aerodynamics Branch, Aerodynamics and Gas Dynamics Division, Mail Stop 499. Associate Fellow AIAA.

Numerical Procedure

A finite volume discretization is applied to the integral form of the Navier–Stokes equations,[11,12] which results in a consistent approximation to the conservation laws governing fluid motion. The spatial domain is divided into a finite number of tetrahedral cells, with each element serving as a computational cell. Thus, the discretized solution to the governing equations results in a set of volume-averaged state variables of mass, momentum, and energy, which are in balance with their area-averaged fluxes (inviscid and viscous) across the cell faces.

Inviscid Fluxes: Cell Reconstruction Scheme

Inviscid flux quantities are computed across each cell face using the Roe[13] flux-difference splitting (FDS) approach (also see Ref. 14) or the Van Leer[15] flux-vector splitting (FVS) technique. Spatial discretization is accomplished by a novel cell reconstruction process, which is based on an analytical formulation for computing solution gradients within tetrahedral cells.

The higher-order reconstruction scheme, derived in Ref. 10 and shown in Fig. 1, is based on a Taylor series expansion of the cell-averaged solution to the cell face. A key component of the scheme is the reconstruction of surrounding cell-averaged data to a common vertex or node by a weighted averaging procedure. Reference 14 proposed a scheme based on an inverse-distance weighted averaging of the primitive variables from the cell centroid to the cell vertices. Whereas this approach has proven to be both accurate and robust through wide application to inviscid problems, it is not fully second-order-accurate in space. It has been shown in Ref. 16 to be approximately 1.85-order accurate.

As development efforts progressed toward solving the Navier–Stokes equations on highly stretched tetrahedral grids, it became evident that the accuracy of the inverse-distance averaging scheme was not adequate. Thus, a fully second-order-accurate averaging procedure was implemented that is based on work by Holmes and Connell[4] and Rausch et al.[17] The procedure is derived by solving a constrained minimization problem to determine weight factors that satisfy Laplacian relationships presented in Ref. 10. The algorithm

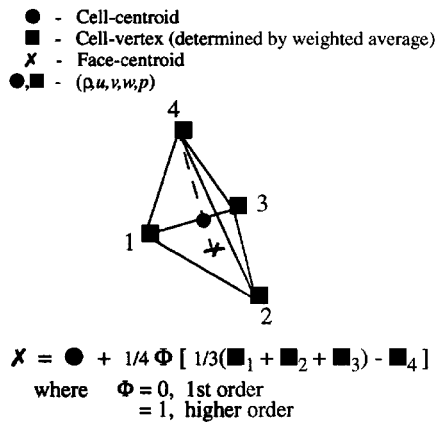

Fig. 1 Reconstruction stencil for tetrahedral cell-centered scheme.

reconstructs to machine accuracy the exact values of a linear function at a node from surrounding cell-centered function values on an arbitrary tetrahedral grid. Furthermore, the simple universal formula shown in Fig. 1 for expanding the cell-centered data to the cell faces also reconstructs the exact value of a linear function to the cell face. Thus, the entire spatial reconstruction scheme is termed second-order accurate, which has been verified by Mitchell.[16]

There is, however, an unresolved shortcoming to the Laplacian-weighted averaging scheme. Each weight factor is assumed to vary by some small perturbation from 1. To achieve an exact reconstruction on highly stretched cells, these perturbations can actually become on the order of one, thus resulting in some negative weight factors. Whereas it can be demonstrated that the computed weight factors produce an exact linear reconstruction, those with negative values violate the principle of positivity, with a detrimental impact on stability during convergence.[18,19] Thus it is necessary to clip the weight factors between 0 and 2, thereby losing some of the exactness of the linear reconstruction but ensuring a more stable scheme.

Viscous Fluxes

The terms in the viscous stress tensor, e.g., τ_{xx}, τ_{xy}, and τ_{xz}, are approximated at the centroids of the cell faces by a linear reconstruction technique that provides a continuous representation of the solution variables across the cell faces. The stencil, presented by Mitchell,[16] utilizes the averaged solution quantity at the three vertices of a cell face, $\boldsymbol{q}_{n1}$, $\boldsymbol{q}_{n2}$, and $\boldsymbol{q}_{n3}$, and the cell-centered values of the two cells sharing the face, $\boldsymbol{q}_{c1}$ and $\boldsymbol{q}_{c2}$, where $\boldsymbol{q} \equiv (\rho, u, v, w, p)$ denotes the primitive variables of density, velocity, and pressure. The derivatives for u, v, w, and temperature T, e.g., u_x, u_y, and u_z, used in the viscous stress terms are derived from a Cramer's rule solution to

$$\begin{bmatrix} x_{c2}-x_{c1} & y_{c2}-y_{c1} & z_{c2}-z_{c1} \\ x_{n2}-x_{n1} & y_{n2}-y_{n1} & z_{n2}-z_{n1} \\ x_{n3}-x_{n2} & y_{n3}-y_{n2} & z_{n3}-z_{n2} \end{bmatrix} \begin{bmatrix} u_x \\ u_y \\ u_z \end{bmatrix} = \begin{bmatrix} u_{c2}-u_{c1} \\ u_{n2}-u_{n1} \\ u_{n3}-u_{n2} \end{bmatrix} \tag{1}$$

Time Integration and Convergence Acceleration

The viscous computations are advanced to steady state by the implicit time-integration algorithm of Ref. 20. The scheme uses the linearized, backward Euler time-differencing approach to update the solution at each time step for the set of equations

$$[\boldsymbol{A}]^n \{\Delta \boldsymbol{Q}\}^n = \{\boldsymbol{R}\}^n \tag{2}$$

where

$$[\boldsymbol{A}]^n = \frac{V}{\Delta t}\boldsymbol{I} + \frac{\partial \boldsymbol{R}^n}{\partial \boldsymbol{Q}}$$

The linear system of equations is solved at each time step with a subiterative procedure, where the tetrahedral cells are grouped into colors (different from face coloring) such that no two cells share a common face.

Thus, the solution is computed by solving for all of the unknowns in a particular color by a point-Jacobi subiteration step before proceeding to the next color. Because the solution of the unknowns for each group can depend on those from previously computed groups, a Gauss–Seidel-like effect is realized. The method has the advantage of being completely vectorizable.

Because of the number of operations required to invert a matrix depends on the matrix bandwidth, the left-hand side of the system of linear equations is evaluated with first-order differencing to reduce both required storage and computer time. Convergence of the subiterations is further accelerated by using Van Leer's FVS on the left-hand side. Thus in the present study, first-order differencing and FVS are applied to the left-hand side and higher-order differencing and FDS to the right-hand side. The viscous Jacobian terms are included on the left-hand side of the equation.

It is necessary to store $[\boldsymbol{A}]^n$, which is a 5×5 matrix for each cell; thus, storage requirements are 180 words/cell for the implicit code. The code requires 84 μs/cell/cycle on a Cray Y-MP, or 37 μs/cell/cycle on a Cray C-90, with 20 subiterations and higher-order differencing. For comparison, the block-structured code CFL3D[21] requires approximately 50 words/cell and 12 μs/cell/cycle on a Cray C-90. Although there may be some room for further improvement in resource requirements of the unstructured code, such codes are typically more computer intensive because of their generalized data structure. The success of this new technology will hinge on reducing the time and expense of generating viscous grids.

Convergence to the steady-state solution is accelerated by sacrificing the time accuracy of the scheme and advancing the equations at each mesh point in time by the maximum permissible time step in that region. Even with such a local time-stepping strategy, experience with solving three-dimensional viscous problems with the present cell-centered scheme has shown that the maximum Courant–Friedrichs–Lewy (CFL) number is limited to approximately 25. This limitation is a consequence of violating the principle of positivity in weighting factors, as noted in an earlier section and in Refs. 18 and 19.

The inherent stability limitation can be improved by scaling the CFL number according to the deviation of cell aspect ratio from the ideal value of an isotropic tetrahedron. This enables the dominant flowfield to evolve quickly with the higher CFL numbers, while restricting the more temperamental viscous cells. A relation has been derived:

$$\Delta t_{\text{corr}} = \Delta t \left[1 - \left(\frac{f_{\Delta t} - 1}{f_{\Delta t}} \right) \left(\frac{1 - \text{AR}}{1 - \text{AR}_{\min}} \right) \right] \tag{3}$$

where $\text{AR} = [9(V_c)^2/(S_{f,\max})^3]/\text{AR}_{\text{ideal}}$, $\text{AR}_{\text{ideal}} = 8/(3\sqrt{3})$, and $f_{\Delta t}$ is a scale factor. V_c is the cell volume, and $S_{f,\max}$ is the area of the largest face of the cell.

The computations presented were performed with a scale factor of $f_{\Delta t} = 6$. Thus, for a prescribed setting of CFL = 150, the actual CFL number will be linearly scaled between 25 for the thinnest tetrahedral cell to 150 for the most isotropic cell. The ultimate benefit of this procedure was a factor-of-two reduction in required solution cycles and, hence, computer time.

Turbulence Model

Spalart–Allmaras

Closure of the Reynolds stress is provided by the one-equation Spalart–Allmaras (S–A) turbulence model.[22] This model is derived using empiricism and arguments of dimensional analysis, Galilean invariance, and selective dependence on the molecular viscosity. The model solves a partial differential equation (PDE) over the entire field for a working variable $\tilde{\nu}$ from which the turbulent eddy viscosity μ_t can be extracted. The PDE is solved separately from the flow equations using the same backward Euler time-integration scheme, which results in a loosely coupled system. The production and destruction terms have been modified as recommended in Ref. 22 to ensure positive eddy viscosity throughout the computation.

On no-slip surfaces, the dependent variable $\tilde{\nu}$ is set to zero. For tangent-flow surfaces, a zero gradient of the variable is applied. Far-field boundary conditions are applied by setting $\tilde{\nu} = 1.341946$ for the inflow, which corresponds to a freestream turbulent kinematic viscosity of $\nu_t = 0.009$, and extrapolating $\tilde{\nu}$ from the interior for outflow boundaries.

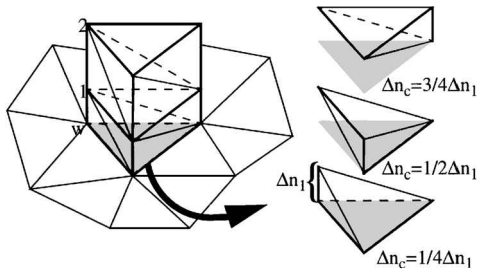

Fig. 2 Inherent structure of thin-layer tetrahedral grids.

The S–A model requires that the distance of each cell to the nearest wall be provided for the near-wall damping terms for cells that are in proximity to viscous surfaces. These distances are determined prior to code execution for cells in the viscous layers and contribute to only a small portion of the overall overhead.

Wall Function

The S–A model has been coupled with a wall function formulation to reduce the need for grid resolving the flow in the sublayer portion of a turbulent boundary layer. With this approach, the inner region of the boundary layer is modeled by an analytical function, which is matched with the numerical solution in the outer region. This has the advantage of 1) significantly reducing memory requirement by eliminating a large portion of cells normally required to resolve the sublayer and 2) improving overall convergence by removing the thinner, more highly stretched cells, which add stiffness to the solution process. A similar approach was successfully demonstrated in Ref. 23, where a two-equation k–ε turbulence model was coupled with a wall function in a modified version of the present code.

The present implementation of a wall function exploits the inherent structure present in viscous unstructured grids produced by the advancing layers method.[9] As evident in Fig. 2, the tetrahedral vertices or nodes are aligned along rays emanating from the surface.

The selected wall function is a law-of-the-wall expression[24] derived by Spalding in 1961. With a single function, it models the inner laminar sublayer, a transition region, and the intermediate logarithmic layer of the turbulent boundary layer:

$$n^+ = u^+ + e^{-\kappa B}\left[e^{\kappa u^+} - 1 - \kappa u^+ - \frac{(\kappa u^+)^2}{2} - \frac{(\kappa u^+)^3}{6}\right] \tag{4}$$

where the nondimensionalized terms are

$$n^+ = \left(\frac{Re_L}{M_\infty}\right)\frac{\rho_w \Delta n u_*}{\mu_w}, \qquad u^+ = \frac{|V|}{u_*}$$

where ρ_w and μ_w are the fluid density and laminar viscosity on the surface, respectively; M_∞ is the freestream Mach number; Re_L is the Reynolds number per reference length L; $|V|$ is the velocity magnitude at an adjacent point located a normal distance Δn away from the surface; u_* is the friction velocity; $\kappa = 0.4$; and $B = 5.5$.

A face-centered slip velocity boundary condition is determined by a two-step process. First, as shown in Fig. 2, ρ_w and μ_w are assigned values from a boundary node, and $|V| \equiv |V_1|$ is defined by the reconstructed velocity magnitude at the first connected node, which is located $\Delta n \equiv \Delta n_1$. Equation (4) is then solved by a Newton–Raphson iteration for u_*, which is assumed to apply at the boundary nodes.

Next the computed friction velocities u_* from three nodes making up a boundary face (shaded surface in Fig. 2) are averaged to establish a face-centered value, and standard face-centered flow boundary condition quantities are prescribed for ρ_w and μ_w . The normal distance to the centroid of the boundary cell is prescribed as $\Delta n_c = \frac{1}{4}\Delta n_1$. With $\Delta n \equiv \Delta n_c$ and the face-averaged value of u_*, Eq. (4) is solved once again by Newton–Raphson iteration for the velocity magnitude, $|V| \equiv |V_c|$. A slip-velocity boundary condition is defined by assigning the new $|V_c|$ to the boundary face and multiplying it with direction cosines extracted from a standard inviscid-type, flow-tangency velocity vector.

A wall boundary condition for turbulent viscosity, which is required by the S–A PDE equation, is computed from a relation presented in Ref. 24,

$$(\nu_t)_w = \nu_w \kappa e^{-\kappa B}\left[e^{\kappa u^+} - 1 - \kappa u^+ - \frac{(\kappa u^+)^2}{2}\right] \tag{5}$$

where $u^+ = |V_c|/u_*$ and $\nu = \mu/\rho$ are determined on the boundary face. The $(\nu_t)_w$ from Eq. (5) is converted to a $\tilde{\nu}$ boundary condition compatible with the governing PDE.[22]

The present implementation considers no adjustment to adiabatic wall density, which is important to high-speed flows. This capability will be added in future work.

A potential shortcoming to the wall function approach arises from the loss of capability to treat laminar regions of the boundary layer. The present implementation assumes fully turbulent flow and introduces turbulence to the domain through a small nonzero inflow quantity. The standard S–A model has the property of remaining dormant in laminar regions and can be turned on either by a tripping function or through natural transition. Thus, the present wall function allows a loss of functionality relative to the standard S–A model. This shortcoming will be addressed in future work by exploring the concept of a switch for each wall point.

Another issue with laminar regions arises at flight Reynolds numbers, where for typical leading-edge shapes of aircraft the thickness of the laminar boundary layer at the leading edge is close to that of the viscous sublayer of the turbulent boundary layers. Thus, resolving the laminar layers becomes as demanding as integrating to the wall for a turbulent boundary layer. Thin-layer grids are currently generated by the VGRIDns code of Ref. 9 with constant normal point distributions across the entire configuration. Work is underway to extend the VGRIDns code to generate viscous grids with variable normal spacing.

Results

Results are presented for the flat-plate boundary-layer problem and the ONERA M6 wing at high-Reynolds-number, transonic, separated flow conditions. The normal grid spacing across the boundary layer is prescribed by the exponential function

$$\Delta n_j = \Delta n_1[1 + a(1 + b)^{j-1}]^{j-1} \tag{6}$$

such that $n_j = n_{j-1} + \Delta n_{j-1}$. The parameter Δn_1 is the spacing of the first node above the surface, and a and b are parameters that control the growth. An initial estimate of the normal point distribution, n^+, etc., is determined by experimenting with parameter variations on an assumed $\frac{1}{7}$th-law velocity profile.

Flat-Plate Boundary Layer

The flat-plate boundary-layer solution is used to assess the accuracy of the wall function in predicting flat-plate turbulent skin friction. The computations were made on quasi-two-dimensional unstructured grids for $M_\infty = 0.5$, $Re_L = 2 \times 10^6$.

Grid 1 was generated by constructing a 49×12 H-topology structured grid with a normal spacing defined by $\Delta n_1 = 0.001L$, $a = 0.3$, and $b = 0.07$ in Eq. (6), which yields roughly five nodes across the boundary layer at $x/L = 0.5$ and an approximate n^+ at the first node of 80. The resulting upper domain boundary ($k = 12$) is located at $0.22L$. The two-dimensional grid was stacked spanwise in $0.02L$ increments to form three planes resulting in a three-dimensional structured dual-channel grid ($49 \times 3 \times 12$) of H–H topology. Each hexahedral cell was subdivided into two prismatic cells, which were further subdivided into three tetrahedra each to form the three-dimensional unstructured grid with 6336 cells. The flat plate was defined by a cosine clustering between the structured indices $15 \le i \le 49$ along the $k = 1$ boundary with inviscid flow prescribed on the $k = 1$ boundary ahead of the plate. Boundary conditions of constant entropy and constant total pressure were prescribed on the inflow plane, whereas an extrapolation condition was applied to the upper and exit domain boundaries. A constant freestream pressure was also imposed on the exit plane.

A second grid was generated in a manner similar to the first to explore the lower limits of grid coarseness on solution accuracy.

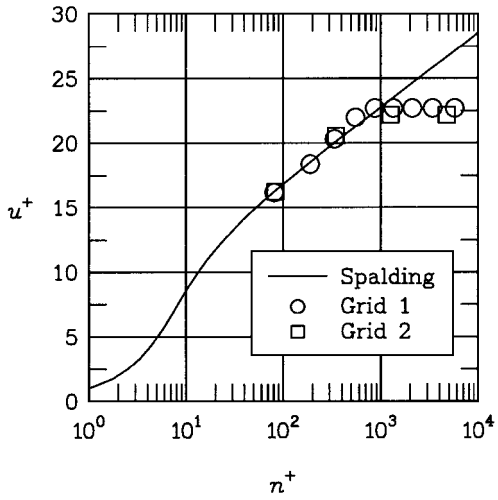

Fig. 3 Effect of grid density on law-of-the-wall behavior for flat-plate boundary-layer flow, $x/L = 0.5$: $M_\infty = 0.5$ and $Re_L = 2 \times 10^6$.

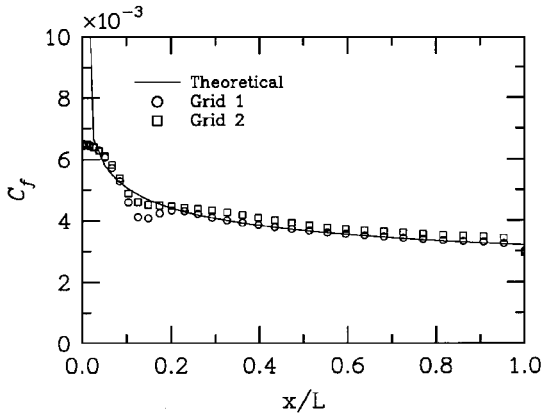

Fig. 4 Effect of grid density on skin-friction coefficient for flat-plate boundary-layer flow: $M_\infty = 0.5$ and $Re_L = 2 \times 10^6$.

Grid 2 was constructed from a 49×6 H topology with the Eq. (6) parameters of $\Delta n_1 = 0.001L$, $a = 2.0$, and $b = 0.07$. This resulted in a three-dimensional channel grid ($49 \times 3 \times 6$) with 2880 cells and an upper domain boundary ($k = 6$) also at $0.22L$.

Figure 3 shows the effect of normal grid density on the law-of-the-wall behavior at $x/L = 0.5$ and $Re_x = 1 \times 10^6$ for the two grids. The plotted nodal solutions were reconstructed from the surrounding tetrahedral cells using the weighted averaging procedure discussed in an earlier section. Note that the first nodal value is matched with the log layer at approximately $n^+ = 80$ for both grids. Grid 1 has five nodes across the boundary layer, whereas grid 2 has three nodes.

The true test of the methodology is reflected in the skin-friction coefficient in Fig. 4. Grid 1 displays excellent agreement over $0.2 < x/L \leq 1.0$ with the theoretical coefficient for fully turbulent flow, $C_f = 0.0583(Re_x)^{-1/5}$, which is based on the $\frac{1}{7}$th-power law assumption. Grid 2 does not exhibit the same level of agreement but is remarkably close considering its extreme grid coarseness across the boundary layer in Fig. 3.

Based on experience with structured-grid computations, one would expect to need between 15 and 40 cells to adequately resolve turbulent boundary-layer flow. Thus, the results of Figs. 3 and 4 require further analysis. As noted earlier, each hexahedral cell is subdivided into two prismatic cells, which are each subdivided further into three tetrahedral cells. For a cell-centered scheme, each tetrahedron functions as one computational cell. Thus, a cell-averaged solution resolves the solution at three vertical positions within each prismatic cell (for a total of six locations within the hexahedral cell). In contrast, a cell-centered structured-grid code,[21] or prismatic unstructured code,[25] would resolve the solution at only one vertical position within their respective cell layers. Hence, in Fig. 3, there are actually three tetrahedral centroids between each plotted solution point (see Fig. 2) that contribute to those points through the reconstruction process mentioned earlier. One can conclude from this discussion that it is more correct to consider the boundary layer as being resolved by 15 cells in grid 1 and 9 cells in grid 2 rather than by five and three nodes, respectively.

One final note. The spurious behavior in the computed skin friction present near the plate leading edge ($0 \leq x < 0.2$) in Fig. 4 may be due to some numerical anomalies of the weighted averaging scheme at the stagnation point where an inviscid surface suddenly changes to a viscous surface. The author plans to revisit this anomaly at a later date. The principal interest for the present study is in the fully developed turbulent flow over the remaining region of the plate.

ONERA M6 Wing

Grid Generation

Tetrahedral viscous and inviscid grids were generated for the ONERA M6 wing using the VGRIDns code.[9] The VGRIDns code is based on the advancing front method (AFM) for generating triangular surface mesh and tetrahedral volume cells.

The distribution of surface and field grid points is controlled by a structured background grid.[26] This transparent grid consists of Cartesian mesh overlaying the entire domain on which the user prescribes point and line sources to impose the desired spacing distribution. Parameters are available to control cell size and the direction and intensity of spatial variation. Cells can be stretched anisotropically in directions of small gradients to reduce the overall grid size. A smooth variation of spacing is achieved throughout the computational domain by solving an elliptic PDE on the Cartesian mesh. The approach is analogous to modeling heat diffusion from discrete heat sources in a conducting medium.

Thin-layered tetrahedra are generated in the viscous regions by the advancing-layers method (ALM), which is based entirely on a modified AFM. The grid is marched away from the surface along smoothed vectors with a user-prescribed distribution function, e.g., Eq. (6). As the cell sizes increase, the Cartesian background grid provides for a smooth transition to the remaining grid, which is generated by the conventional AFM.

The marching process of the ALM produces prismatic-like layers of grid, which are subdivided into three tetrahedra within each prism, as shown in Fig. 2. As with the flat-plate boundary-layer grids, each prismatic base cell is resolved spatially by three computational cells for a tetrahedral cell-centered scheme.

Test Matrix

Several tetrahedral grids, eight thin layered and one conventional, were generated for the ONERA M6 wing (Tables 1 and 2). The spatial sources for the background grid were prescribed to produce a coarse (6483 triangles) and a fine (8956 triangles) surface grid distribution on the wing (Fig. 5) and remained unchanged thereafter. Anisotropic stretching of the surface grids was applied in the spanwise direction to reduce the total number of required cells while maintaining good chordwise resolution. A typical off-body distribution of volume grid for the coarse mesh is indirectly reflected in Fig. 6 by the centerplane grid of the WF2-6(C) configuration. Note the smooth transition from the layered viscous grid to the conventional inviscid grid. As is evident in Fig. 6, the grid has characteristics of a structured O mesh because clustering of cells in the wake region has not been applied. Wake clustering is a topic for future research.

Table 1 Designations for ONERA M6 viscous tetrahedral grids

Initial spacing $(\Delta n_1/c_{ROOT}) \times 10^4$	Nominal midchord n^+	Number of cells (nodes) across boundary layer: ≈12 cells (4 nodes)	≈18 cells (6 nodes)	≈30 cells (10 nodes)
0.6	4	——	FV-8[a]	——
1.350	50	——	WF1-6	——
2.025	70	WF2-4	WF2-6(C,F)	WF2-10
4.050	150	——	WF4-6	——
6.075	220	——	WF6-6	——

[a]Includes two additional points in the inner layer.

Table 2 Parameters and characteristics of viscous grids

Grid	a [see Eq. (6)]	b [see Eq. (6)]	Number of surface triangles	Number of cells N_{cell}	$(N_{cell})_{Viscous}/(N_{cell})_{Inviscid}$
Inviscid	——	——	6,483	258,768	——
FV-8	0.5	0.07	6,483	414,038	1.60
WF1-6	0.95	0.07	6,483	356,093	1.38
WF2-4	2.2	0.00	6,483	324,356	1.25
WF2-6(C)	0.8	0.07	6,483	356,472	1.38
WF2-10	0.2	0.07	6,483	463,968	1.79
WF4-6	0.56	0.07	6,483	359,268	1.39
WF6-6	0.432	0.07	6,483	362,311	1.40
WF2-6(F)	0.8	0.07	8,956	578,556	——

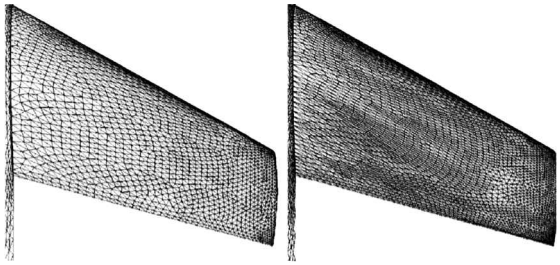

Fig. 5 Upper surface triangulation of ONERA M6 wing; left, coarse grid, 6483 triangles on wing surface; and right, fine grid, 8956 triangles on wing surface.

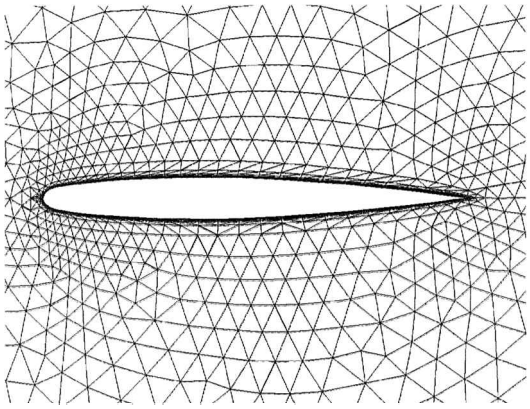

Fig. 6 Center plane triangulation of ONERA M6 wing, coarse grid, WF2-6(C).

Full viscous (FV) with grid-resolved sublayer and wall function (WF) with non-grid-resolved sublayer values, respectively, are given in Tables 1 and 2. The numerical nomenclature, e.g., 2-6, provides a nominal indicator of the initial spacing (2) and number of nodes across the boundary layer (6) at the 0.5 mean aerodynamic chord for a $Re_{mac} = 11.7 \times 10^6$.

The FV-8 grid was designed to have approximately the same number of nodes in the outer layer of the boundary layer as the WF2-6 grid, i.e., six nodes (18 tetrahedral layers), plus two additional nodes in the sublayer, for a total of eight nodes (24 tetrahedral layers). The nominal n^+ for the first node above the surface at a typical midchord station ranged from 50 to 220 for the WF grids and had a value of 4 for the FV grid.

A conventional inviscid grid was generated from the same wing surface grid and with the same spatial source distributions as the viscous grids, thus, serving as a reference for measuring the additional cell requirements for viscous grids, as shown in Table 2. Note that the viscous grids require from 25% for the WF2-4 with 324,356 cells (57,490 nodes) to 79% for the WF2-10 with 463,968 cells (80,927 nodes) more tetrahedral cells than the standard inviscid unstructured grid. It is obvious from Table 2 that grid size can become rather large if more cells are needed across the boundary layer. This factor highlights the strong need for techniques, such as a WF, to keep the viscous overhead down to manageable levels.

Table 3 Resource requirements for unstructured cases

Grid	Number of cycles	Cray C-90 time, h	Memory, Mwords
Inviscid	300	0.6	46
FV-8	900/425	5.9[a]	75
WF1-6	1500	5.78	64
WF2-4	900	3.05	59
WF2-6(C)	2000	7.34	64
WF2-10	2500	12.38	84
WF4-6	1500	5.75	65
WF6-6	1500	5.88	66
WF2-6(F)	2500	15.53	104

[a]Obtained with mesh sequencing.

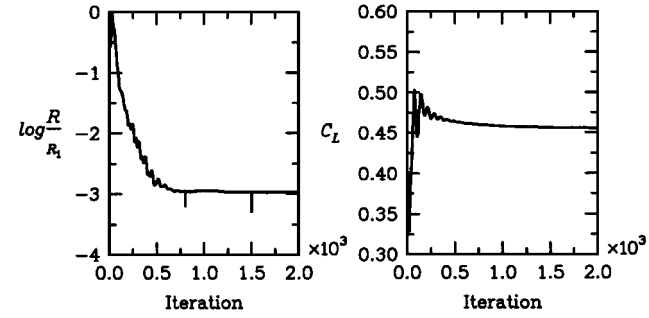

Fig. 7 Solution convergence history for WF2-6(C): $M_\infty = 0.8447$, $\alpha = 5.06$ deg, and $Re_{mac} = 11.7 \times 10^6$.

A structured-grid computation was repeated from Ref. 21 for comparison with the unstructured results. The grid consisted of a $193 \times 49 \times 33$ C–O mesh (294,912 hexahedral cells) with a minimum normal spacing over the wing of $0.000015c_{ROOT}$. This spacing matches that of the centroid of the surface tetrahedral cells in the FV-8 grid. Reference 21 reports that this initial spacing resulted in an average n^+ of 4 over the wing for $M_\infty = 0.84$, $\alpha = 3.06$ deg, and $Re_{mac} = 11.7 \times 10^6$.

Solution Convergence

All turbulent flow computations were performed at the flow conditions of $M_\infty = 0.8447$, $\alpha = 5.06$ deg, and $Re_{mac} = 11.7 \times 10^6$, which represents a high-Reynolds-number, transonic, separated flow condition. A typical solution convergence is shown in Fig. 7.

The reason for the leveling off of the residual curve at a three-order-of-magnitude reduction is not fully understood, but it may be due to an unsteady nature of complex flow separation in the wing–tip region. Note that the lift coefficient sets up quickly, but it is necessary to run the solution longer to allow for the separated region to evolve fully.

Resource requirements for the computations are presented in Table 3. All of the viscous cases were run with CFL numbers starting at 20 and ramping up to 150 over 20 cycles. The computations include the cell aspect-ratio-based variable CFL scaling strategy of Eq. (3) with a $f_{\Delta t} = 6$ applied. The time for the FV-8 case is based on mesh sequencing, which will be described in a later section. Unresolved difficulties were encountered while attempting to start the FV case from freestream initial conditions.

The structured-grid computation was performed with CFL3D using a multigrid strategy. The solution was converged in 500 cycles and required 16 Mwords and 0.66 h using the Cray C-90.

Surface Flow Characteristics

Figure 8 shows the surface flow patterns for the FV-8 case, which reveals a substantial shock-induced separation on the outboard portion of the wing. These patterns were determined from the reconstructed velocities at the first node above the wing surface. The general pattern shown in Fig. 8 is also representative of that from all of the WF-series WF solutions.

Surface Grid Sensitivity

Figure 9 shows the effect of surface grid density on the chordwise C_p distributions at four chord stations corresponding to those

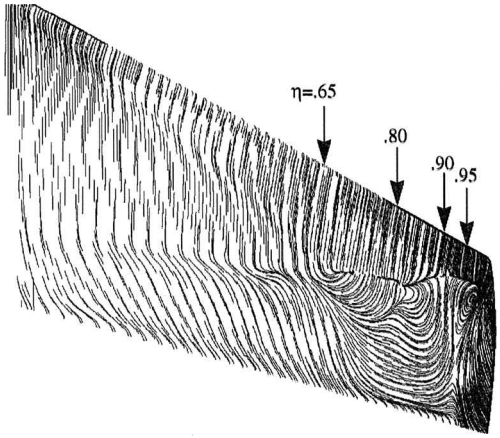

Fig. 8 Surface oil-flow patterns for ONERA M6 wing, FV-8 grid: M_∞ = 0.8447, α = 5.06 deg, and Re_{mac} = 11.7 × 10⁶.

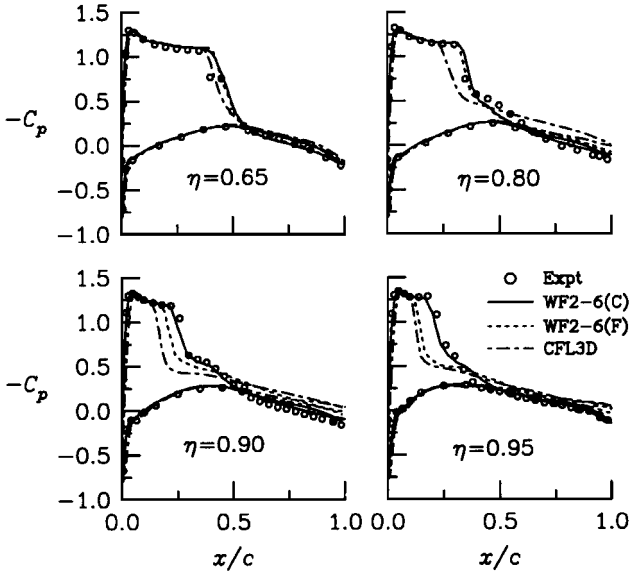

Fig. 9 Effect of surface grid density on C_p distributions for ONERA M6 wing: M_∞ = 0.8447, α = 5.06 deg, and Re_{mac} = 11.7 × 10⁶.

shown in Fig. 8 in comparison with the experimental data of Ref. 27. The WF2-6(C) and (F) have differing surface grids (see Fig. 5) but identical normal grid spacings across the boundary layer. Included for reference is a structured-grid solution obtained from the CFL3D code.[21] The sensitivity to unstructured surface grid resolution is small at the $\eta = 0.65$ and 0.80 stations, where the flow separation is shown to be more well behaved in Fig. 8. Significant differences in shock location are observed for the WF solutions in the more complex flow region for $\eta \geq 0.90$. The structured-grid CFL3D and finer unstructured-grid WF2-6(F) solutions both predict the outer shock location ahead of the experimental result. Reference 21 also reports additional sensitivities of the tip region flow to the selection of turbulence model. Because significant sensitivities in the tip region flow can arise from a variety of sources, it was decided to use the coarser surface grid to study the incremental effects of parametric variations in normal grid spacing to reduce the overall computational expense of running a matrix of cases.

Validation of WF

Figure 10 shows a comparison of longitudinal C_p distributions for unstructured FV and WF solutions and a reference unstructured inviscid result. Note that the inviscid C_p distributions clearly show the strong viscous effects present on this configuration and highlight the necessity of modeling those effects. Only small differences are observed between the FV near-wall modeling FV-8 and the WF approach WF2-6(C). This result serves to increase confidence in the applicability of the WF to transonic, separated flows.

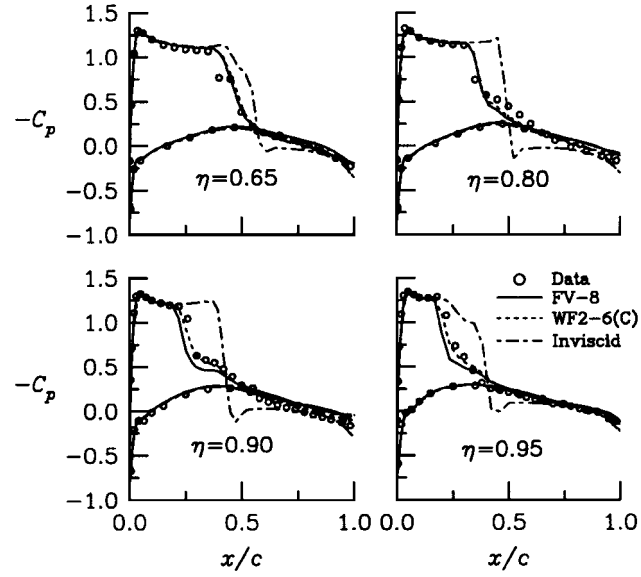

Fig. 10 Effect of wall function on predicting C_p distributions for ONERA M6 wing: M_∞ = 0.8447, α = 5.06 deg, and Re_{mac} = 11.7 × 10⁶.

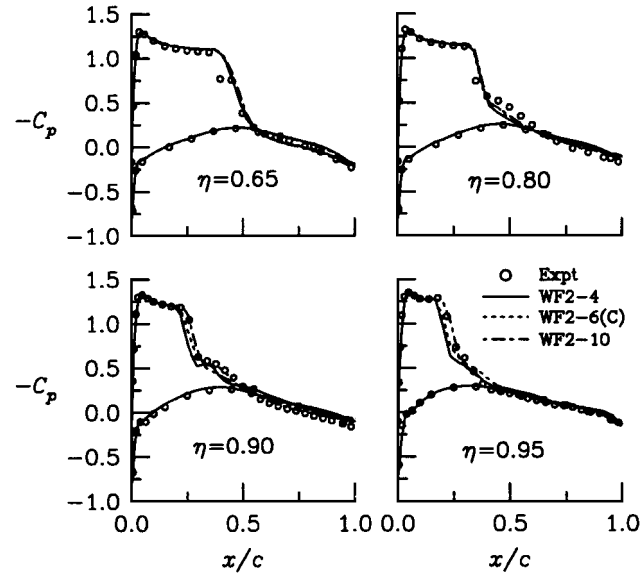

Fig. 11 Effect of normal grid density on C_p distributions for ONERA M6 wing: M_∞ = 0.8447, α = 5.06 deg, and Re_{mac} = 11.7 × 10⁶.

Normal Grid Density

Figure 11 shows the effect of normal grid density (a horizontal cut across Table 1) on the chordwise C_p distributions at four chord stations. The three solutions, which represent 12, 18, and 30 cells across the boundary layer, are generally in good agreement with each other and the experimental data.

The law-of-the-wall behavior of the boundary layer for an attached flow region of the wing ($x/c = 0.5$, $2y/b = 0.15$) is plotted in Fig. 12. The fixed initial spacing yields $n^+ = 71$ for all three cases, whereas there are 4, 6, and 10 nodes across the boundary-layer corresponding to WF2-4, WF2-6, and WF2-10, respectively. Recall that there are three tetrahedra between each nodal point contributing to the reconstruction of the solution to the nodes (as shown in Fig. 2).

Effect of Initial Grid Spacing

Figure 13 shows the effect of initial grid spacing (a vertical cut through the WF series of Table 1) on the chordwise C_p distributions at four chord stations. Each grid is sized to have approximately six nodes (18 tetrahedra) across the boundary layer at the midchord of the mean aerodynamic chord. For the test flow conditions, the initial grid spacings yield an n^+ of 48, 71, 146, and 218 for the first node of

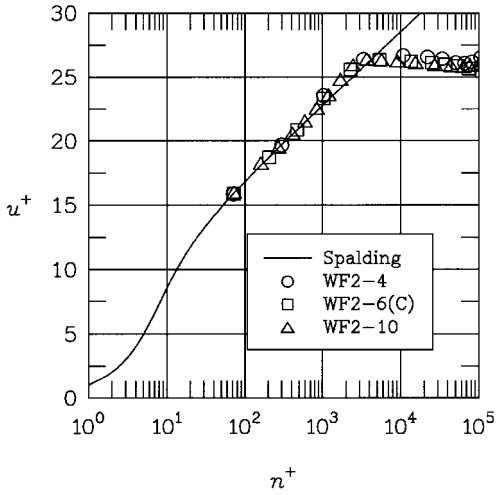

Fig. 12 Effect of normal grid density on law-of-the-wall behavior at $x/c = 0.5$, $2y/b = 0.15$ for ONERA M6 wing: $M_\infty = 0.8447$, $\alpha = 5.06$ deg, and $Re_{mac} = 11.7 \times 10^6$.

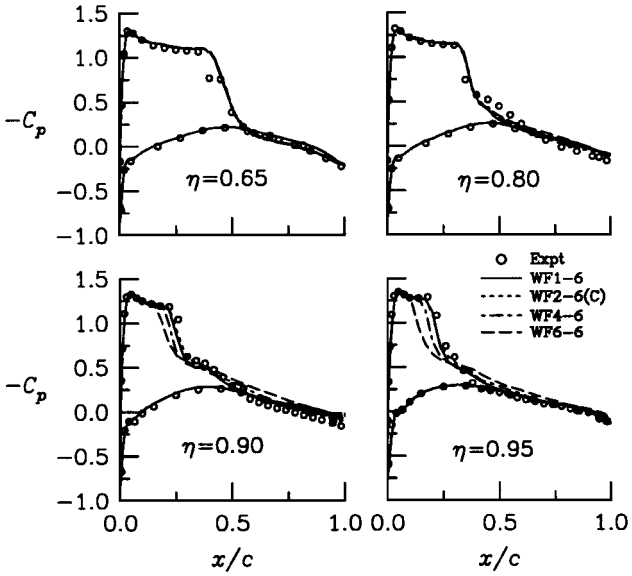

Fig. 13 Effect of initial nodal spacing on C_p distributions for ONERA M6 wing: $M_\infty = 0.8447$, $\alpha = 5.06$ deg, and $Re_{mac} = 11.7 \times 10^6$.

the WF1-6, WF2-6, WF4-6, and WF6-6, respectively, at $x/c = 0.5$, $2y/b = 0.15$. The sensitivity to initial spacing is negligible for all cases at the $\eta = 0.65$ and 0.80 stations and for WF1-6 and WF2-6 at $\eta = 0.90$ and 0.95. As might be expected, the agreement with data deteriorates at the higher values of n^+ for $\eta \geq 0.90$. This result suggests that fairly large values of n^+ can be applied in conjunction with a WF for more well-behaved separated flows. However, more restricted values should be used in regions with complex three-dimensional separated flow structures, such as spiral separations or primary saddle points, as shown in Fig. 8.

General Guidelines

The preceding results suggest that general guidelines can be established for future applications of this unstructured Navier–Stokes methodology. As a rule of thumb for utilizing the WF on cases that may exhibit flow separation, the author recommends normal grid distributions similar to that of the WF1-6 grid; i.e., at a representative midchord location prescribe spacings that yield approximately six nodes (18 tetrahedra) across the boundary layer with an initial nodal n^+ of 50.

Mesh Sequencing

The mesh sequencing strategy is often employed as a means of accelerating solution convergence. This strategy involves establishing the primary flowfield relatively quickly around a configuration using a coarse mesh and then transferring that solution onto a finer mesh to complete the final grid-resolved solution.

Table 4 Resource requirements for mesh sequencing from coarse grid, WF2-4

Finer grid	Cray C-90 h for interpolating solution	Additional cycles beyond WF2-4	Total Cray C-90 solution time, h	Savings, %
WF2-6(F)	2.1	700	9.5	39
WF2-10	2.4	300	6.9	44
FV-8	1.1	425	5.9	——

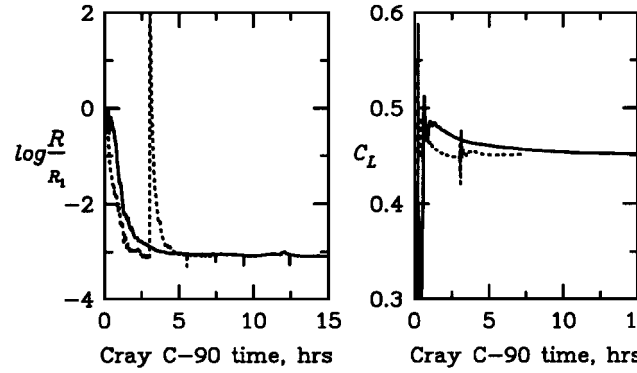

Fig. 14 Effect of mesh sequencing on solution convergence for WF2-6(F) grid: ——, single-grid solution, and - - - -, mesh-sequenced solution; $M_\infty = 0.8447$, $\alpha = 5.06$ deg, and $Re_{mac} = 11.7 \times 10^6$.

A demonstration of this procedure is provided for two of the more costly WF solutions from Table 3, WF2-6(F) and WF2-10, and for the FV case, FV-8. Figure 14 compares computer time requirements (in Cray C-90 hours) to obtain convergence of residual error and lift coefficient for the WF2-6(F) mesh. The solid curve applies to the single-grid computation, which took 15.5 h on the Cray C-90 for 2500 cycles. The dashed line denotes the application of mesh sequencing, starting from the coarse-grid WF2-4 solution at 900 cycles (see Table 3), interpolating that solution onto the WF2-6(F) grid, and continuing to run for another 700 cycles with CFL = 150. The history plots in Fig. 14 do not reflect the additional computer time used for interpolating the solution from coarse to fine mesh.

The full benefit of mesh sequencing is presented in Table 4 for the three candidate cases, including the overhead of interpolating solutions. Note that the total savings is on the order of 40–45% for the cases shown. (A savings is not included for the FV-8 because of difficulties in obtaining a single-grid solution for that case.) An additional benefit is derived from the lower memory usage of the coarse-grid solution (59 Mwords for the WF2-4), thus enabling primary flow to be set up more quickly while running in smaller queues on heavily used computers.

Concluding Remarks

A systematic study has been initiated to assess the utilization of the cell-centered unstructured scheme for obtaining accurate solutions to the Navier–Stokes equations on three-dimensional configurations in an efficient manner. Closure to the flow equations is provided by a one-equation S–A turbulence model, which is coupled with a WF.

Excellent accuracy in predicting the law-of-the-wall behavior and surface skin-friction coefficient with tetrahedral cells was demonstrated for the flat-plate boundary-layer problem. The applicability of the tetrahedral-based WF approach to three-dimensional, high-Reynolds-number, transonic, separated flow was validated on a parametric set of grids for the ONERA M6 wing. The validations were supported by comparisons with experimental data and a companion structured-grid solution. The parametric study revealed that reasonable viscous solutions can be obtained with approximately 25–80% more cells, hence memory, than a standard anisotropically stretched inviscid grid. Guidelines are established for prescribing an efficient

distribution of normal grid spacing. A 40–45% solution convergence acceleration was demonstrated using a mesh sequencing strategy.

Although the present study concludes with useful guidelines and better understanding of the base methodology, the next step of applying this knowledge to more complex geometries is important. Work is currently underway toward that end.

Acknowledgments

The author would like to thank Shahyar Pirzadeh, Configuration Aerodynamics Branch, NASA Langley Research Center (LaRC), for generating the tetrahedral grids used in this study. The support of Paresh Parikh, Paragon Research, Inc., in performing the solution interpolations for mesh sequencing is gratefully acknowledged. The author wishes to thank Christopher L. Rumsey, Aerodynamic and Acoustic Methods Branch (AAMB) at NASA LaRC, for providing the supporting structured grid and flow solver. The consultation and advice of W. Kyle Anderson, AAMB at NASA LaRC, toward implementing the Spalart–Allmaras turbulence model is acknowledged and greatly appreciated. The computations were performed on the numerical aerodynamic simulation facility and the Aeronautics Consolidated Supercomputing Facility at NASA Ames Research Center and on the Cray Y-MP at NASA LaRC.

References

[1]Anderson, W. K., and Bonhaus, D. L., "An Implicit Upwind Algorithm for Computing Turbulent Flows on Unstructured Grids," *Computers and Fluids*, Vol. 23, No. 1, 1994, pp. 1–21.

[2]Barth, T. J., and Linton, S. W., "An Unstructured Mesh Newton Solver for Compressible Fluid Flow and Its Parallel Implementations," AIAA Paper 95-0221, Jan. 1995.

[3]Chalot, F., Mallet, M., and Ravachol, M., "A Comprehensive Finite Element Navier–Stokes Solver for Low- and High-Speed Aircraft Design," AIAA Paper 94-0814, Jan. 1994.

[4]Holmes, D. G., and Connell, S. D., "Solution of the 2D Navier–Stokes Equations on Unstructured Adaptive Grids," *AIAA 9th Computational Fluid Dynamic Conference*, AIAA, Washington, DC, 1989, pp. 25–39; also AIAA Paper 89-1932, June 1989.

[5]Mavriplis, D. J., "A Three Dimensional Multigrid Reynolds-Averaged Navier–Stokes Solver for Unstructured Meshes," NASA CR-194908, May 1994.

[6]Marcum, D. L., and Agarwal, R. K., "A Three-Dimensional Finite Element Flow Solver with k–ε Turbulence Model for Unstructured Grids," AIAA Paper 90-1652, June 1990.

[7]Nakahashi, N., "FDM-FEM Zonal Approach for Viscous Flow Computations over Multiple Bodies," AIAA Paper 87-0604, Jan. 1987.

[8]Ward, S., and Kallinderis, Y., "Hybrid Prismatic Tetrahedral Grid Generation for Complex 3-D Geometries," AIAA Paper 93-0669, Jan. 1993.

[9]Pirzadeh, S., "Viscous Unstructured Three-Dimensional Grids by the Advancing-Layers Method," AIAA Paper 94-0417, Jan. 1994.

[10]Frink, N. T., "Recent Progress Toward a Three-Dimensional Unstructured Navier–Stokes Flow Solver," AIAA Paper 94-0061, Jan. 1994.

[11]Warsi, Z. U. A., *Fluid Dynamics—Theoretical and Computational Approaches*, CRC Press, Boca Raton, FL, 1993, p. 101.

[12]Frink, N. T., "Assessment of an Unstructured-Grid Method for Predicting 3-D Turbulent Viscous Flows," AIAA Paper 96-0292, Jan. 1996.

[13]Roe, P. L., "Characteristic Based Schemes for the Euler Equations," *Annual Review of Fluid Mechanics*, Vol. 18, 1986, pp. 337–365.

[14]Frink, N. T., "Upwind Scheme for Solving the Euler Equations on Unstructured Tetrahedral Meshes," *AIAA Journal*, Vol. 30, No. 1, 1992, pp. 70–77.

[15]Van Leer, B., "Flux-Vector Splitting for the Euler Equations," *Eighth International Conference on Numerical Methods in Fluid Dynamics*, edited by E. Krause, Vol. 170, Lecture Notes in Physics, Springer–Verlag, Berlin, 1982, pp. 507–512.

[16]Mitchell, C. R., "Improved Reconstruction Schemes for the Navier–Stokes Equations on Unstructured Meshes," AIAA Paper 94-0642, Jan. 1994.

[17]Rausch, R. D., Batina, J. T., and Yang, H. T. Y., "Spatial Adaption Procedures on Unstructured Meshes for Accurate Unsteady Aerodynamic Flow Computation," AIAA Paper 91-1106, April 1991.

[18]Barth, T. J., "Numerical Aspects of Computing Viscous High Reynolds Number Flows on Unstructured Meshes," AIAA Paper 91-0721, Jan. 1991.

[19]Coirier, W. J., "An Adaptively-Refined, Cartesian, Cell-Based Scheme for the Euler and Navier–Stokes Equations," NASA TM-106754, Oct. 1994.

[20]Anderson, W. K., "Grid Generation and Flow Solution Method for Euler Equations on Unstructured Grids," NASA TM-4295, April 1992.

[21]Rumsey, C. L., and Vatsa, V. N., "A Comparison of the Predictive Capabilities of Several Turbulence Models Using Upwind and Central-Difference Computer Codes," AIAA Paper 93-0192, Jan. 1993.

[22]Spalart, P. R., and Allmaras, S. R., "A One-Equation Turbulence Model for Aerodynamic Flows," AIAA Paper 92-0439, Jan. 1992.

[23]Kwon, O. J., and Hah, C., "Solution of the 3-D Navier–Stokes Equations with a Two-Equation Turbulence Model on Unstructured Meshes Applied to Turbomachinery," AIAA Paper 94-1833, June 1994.

[24]White, F. M., *Viscous Fluid Flow*, McGraw–Hill, New York, 1974, p. 475.

[25]Khawaja, A., McMorris, H., and Kallinderis, Y., "Hybrid Grids for Viscous Flows Around Complex 3-D Geometries Including Multiple Bodies," AIAA Paper 95-1685, June 1995.

[26]Pirzadeh, S., "Structured Background Grids for Generation of Unstructured Grids by Advancing-Front Method," *AIAA Journal*, Vol. 31, No. 2, 1993, pp. 257–265.

[27]Schmitt, V., and Charpin, F., "Pressure Distributions on the ONERA M6-Wing at Transonic Mach Number," AGARD Advisory Rept. 138, May 1979.

D. S. McRae
Associate Editor